Chapter-5

$Ni_{0.5}Co_{0.5}S$ Nano-Chains: A High Performing Pseudocapacitive Electrode for Hybrid Supercapacitors

Chapter-5

$Ni_{0.5}Co_{0.5}S$ Nano-Chains: A High Performing Pseudocapacitive Electrode for Hybrid Supercapacitors

5.1 Introduction

Because of its unique and distinctive properties, nickel sulfide is helpful in various applications and can serve as both the cathode and anode material for LIBs. [1, 2] Cobalt sulfides have been investigated as robust materials for use in LIBs as cathodes with low overpotential, long cycle life, great resilience, and durability. [3, 4] Bimetallic sulfides have excellent electrochemical activity and capacity when compared to most mono-metal sulfides. For the same reason bimetallic sulfides have been considered a viable class of electrode materials for high-performance energy storage devices. [5-10] Ni-Co-S compounds with various stoichiometric compositions, such as $NiCo_2S_4$, [11-14] $CoNi_2S_4$, [15-17] $Ni_{1.5}Co_{1.5}S_4$, [18, 19] $Ni_xCo_{3-x}S_4$,[20, 21] $(Ni_{0.5}Co_{0.5})_9S_8$, [22] and $Ni_xCo_{1-x}S_2$ [23-25] have attracted significant attention due to their distinct physical, chemical, electrical and optical characteristics. They find numerous potential applications in catalysis and electrochemical supercapacitors.

Electrochemical activities can be maximized by altering the active material compositio ns, fine-tuning the electronic structures and adjusting the active sites of materials. The ionic radius of Co^{2+} is close to that of Ni^{2+} as they are adjacent transition metal elements. Thus, the doping of Ni into CoS can regulate the electronic structure and stabilizes Co species as electrode material for supercapacitors. As the crystal structure and ionic radius are similar, a solid solution of $Ni_xCo_{1-x}S$ is expected to be formed. C Huang *et al.* for the very first time tried and prepared bundle-like $Ni_xCo_{1-x}S$/C nanostructures by

using three dimensional Ni-Co-BTC as a precursor for enhanced supercapacitors. [26] This chapter presents the synthesis and characterizations of a bimetallic sulfide $Ni_{0.5}Co_{0.5}S$ nanostructures. It also deals with the electrochemical performances of the developed $Ni_{0.5}Co_{0.5}S$ nano-chains electrodes. Among the significant results, $Ni_{0.5}Co_{0.5}S$ electrode exhibited a highly improved electrochemical performance as they leverage the combined advantages of Co/Ni-S electronic structures. The sample electrode achieved the capacitance equivalent to 2378 F/g at 1 mV/s while a specific capacity of 2190 F/g at 1 A/g in 4 M KOH aqueous electrolyte. Furthermore, an impressive energy density equivalent to ~257 Wh/kg and power density of ~7.2 kW/kg was achieved by the assembled $Ni_{0.5}Co_{0.5}S$//AC aqueous asymmetric supercapacitors (ASCs) where $Ni_{0.5}Co_{0.5}S$ electrode as the positive electrode and activated carbon (AC) was employed as the negative electrode.

5.2 Experimental:

5.2.1 Synthesis Method

All chemicals used in this experiment were purchased from Alfa-Aesar and used without any further purification. $NiCl_2.6H_2O$ and $CoCl_2.6H_2O$ with equal molar ratios of 1:1 were dissolved in 250 ml deionized water with continuous stirring for 5-6 hrs and ultrasonicated for 30 min respectively to make a homogeneous solution, followed by passing H_2S gas (synthesized by the Kipp generator method) into the solution. A schematic illustration of the synthesis of $Ni_{0.5}Co_{0.5}S$ is shown in Fig. 5.1.

The obtained fine precipitate was then filtered and washed several times with deionized water and ethanol. Then the product was dried in a hot air oven (under an N_2 atmosphere) at 120 °C for 24 hours and used for crystallographic and electrochemical characterizations. The chemical reaction representing the formation of $Ni_{0.5}Co_{0.5}S$ is given below in equation 5.1.

$$CoCl_2.6H_2O + NiCl_2.6H_2O + 2H_2S \rightarrow 2Ni_{0.5}Co_{0.5}S + 12H_2O + 4HCl \qquad (5.1)$$

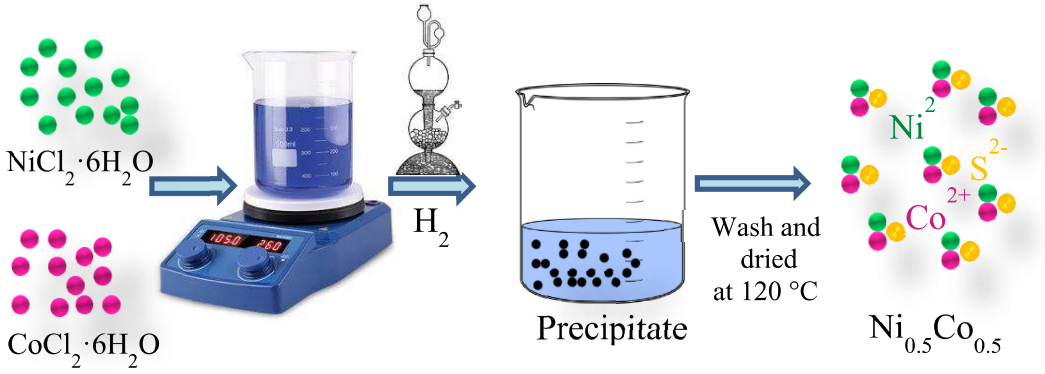

Fig. 5.1 Schematic illustration of the synthesis of $Ni_{0.5}Co_{0.5}S$.

5.3 Results and Discussions:

5.3.1 XRD Studies

Single-phase hexagonal $Ni_{0.5}Co_{0.5}S$ sample was synthesized using a simple H_2S-mediated two-phase (gas diffusion in liquid) precipitation route in an aqueous medium. $Ni_{0.5}Co_{0.5}S$ formed in a single phase due to the gradual diffusion of H_2S gas into the liquid phase resulting in controlled precipitation of the solid phase. Fig. 5.2a shows the Rietveld refined XRD profile of the hexagonal $Ni_{0.5}Co_{0.5}S$. The crystal structure was refined using hexagonal CoS as the model structure. The sharp prominent diffraction peaks at 2θ values 30.67, 35.34, 46.95, 54.52, 62.56, 63.87, 66.65, 73.12 and 74.75 represent the (100), (101), (102), (110), (103), (200), (201), (004) and (202) planes, respectively of $Ni_{0.5}Co_{0.5}S$ in the hexagonal cell (space group: $P6_3/mmc$) with lattice parameters a = b = 3.37 (1) Å, c = 5.18 (3) Å, α = β = 90° and γ = 120° matches very well with the diffraction peaks of hexagonal CoS (ICDD File No: 01-075-0605). The VESTA image of the $Ni_{0.5}Co_{0.5}S$ nano-chains in a layered hexagonal structure is shown in Fig. 5.2b. Crystallite size was evaluated using the Debye-Scherrer equation and the average crystallite size was found to be ~21.07 (±1) nm. Due to the replacement of smaller Co^{2+} ions (r_{Co2+} = 0.065 nm) by the larger Ni^{2+} ions (r_{Ni2+} = 0.069 nm) in the

hexagonal CoS structure, lattice parameters of $Ni_{0.5}Co_{0.5}S$ are shifted to a higher value than those of hexagonal CoS. [25] Thus XRD pattern of the powder sample confirms the phase purity and formation of the single-phase hexagonal (space group: $P6_3/mmc$) $Ni_{0.5}Co_{0.5}S$ nano-chains as diffractions for no secondary phase are observed in XRD patterns.

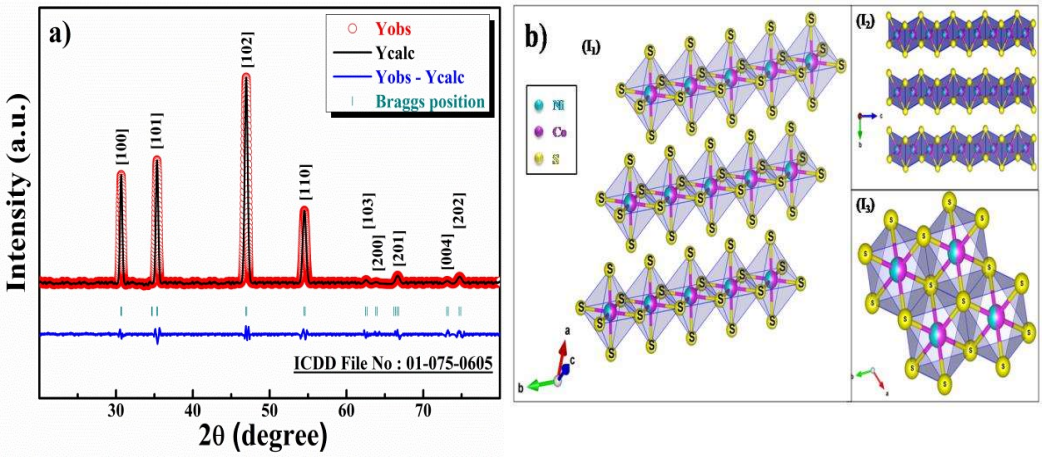

Fig. 5.2 (a) Shows Rietveld refinement of the XRD profile and **(b)** VESTA image of $Ni_{0.5}Co_{0.5}S$ nano-chains.

5.3.2 Thermal Analysis

The thermal stability of the sample was studied using thermogravimetric analysis (TGA) in an N_2 environment, as shown in Fig. 5.3a. The black powder of $Ni_{0.5}Co_{0.5}S$ sample was heated from room temperature to 700 °C at a rate of 10 °C min^{-1}. There were two stages of weight loss for the $Ni_{0.5}Co_{0.5}S$ nano-chains. The first weight loss stage is located around 65-135 °C (weight loss of about 6%, equivalent to ~ 0.45 H_2O molecule) due to the removal of physically adsorbed moisture and the hydroxide group. From 135 °C to 533 °C, the sample is almost stable, with a slight weight loss which implies that the $Ni_{0.5}Co_{0.5}S$ nano-chains are stable to a fairly high temperature. After 533 °C, there is a sudden weight loss because of the decomposition of the $Ni_{0.5}Co_{0.5}S$ nano-chains with the evolution of sulfur in which the weight loss of about 19.6% was observed. [27, 28] Hence the sample was dried at 120°C in an N_2 atmosphere to make

it moisture free for studying the electrochemical performances of the electrode. The weight losses that appeared in the TGA study are represented by equations

$$Ni_{0.5}Co_{0.5}S.xH_2O \rightarrow Ni_{0.5}Co_{0.5}S + xH_2O \quad ; x\sim 0.45 \quad (T \sim 135\ ^oC) \quad (5.2)$$

$$Ni_{0.5}Co_{0.5}S \rightarrow Ni_{0.5}Co_{0.5}S_x + (1\text{-}x)\ S \quad ; x\sim 0.45 \quad (T \sim 550\ ^oC) \quad (5.3)$$

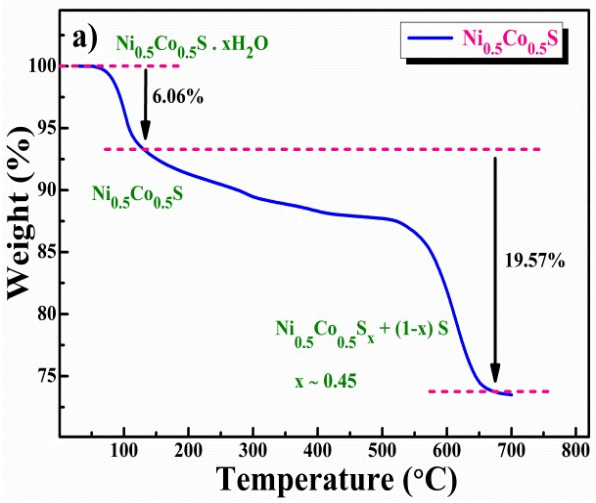

Fig. 5.3 (a) TGA of $Ni_{0.5}Co_{0.5}S$ nano-chains in an N_2 atmosphere

5.3.3 Structural Analysis

The FT-IR spectrum of the as-prepared (without any pre-heating) $Ni_{0.5}Co_{0.5}S$ nano-chains is shown in Fig. 5.3b. The broad band at 3347 and 1631 cm^{-1} corresponds to the stretching and bending vibrations of the OH functional group of water adsorbed to the surface, respectively. The bands at 407, 414, 421 and 433 cm^{-1} are related to the symmetrical stretching vibration whereas 1016 and 1085 cm^{-1} are related to the asymmetrical stretching vibration assigned to Ni-S or Co-S bonds in $Ni_{0.5}Co_{0.5}S$ sample. [29, 30]

For additional investigation on the structure and phase composition of the sample, Raman spectroscopy was performed on pre-heated active material shown in Fig. 5.3c. Peaks at 180, 455, 513 and 640 cm^{-1} can be indexed to the Raman-active vibrational peaks of $Ni_{0.5}Co_{0.5}S$ sample which correspond to the typical phonon modes F_{2g}, E_g, T_{2g}

and A_{1g} respectively. [31, 32] Raman lines for the $Ni_{0.5}Co_{0.5}S$ sample were shifted toward lower wave numbers, i.e., bathochromic shift or red-shift indicating the phonon confinement effect (quantum confinement of optical phonons) supported by the high-intensity stretching band at 962 cm^{-1}. [29]

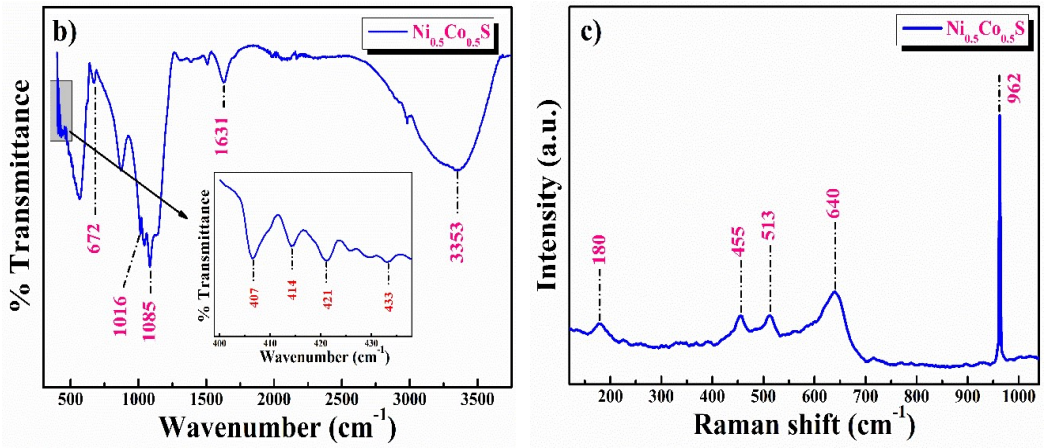

Fig. 5.3 (b) FT-IR spectra and **(c)** Raman spectra of $Ni_{0.5}Co_{0.5}S$ nano-chains

5.3.4 Bandgap Measurement and Surface Area Analysis

The UV-visible absorption spectrum of as-synthesized pre-heated $Ni_{0.5}Co_{0.5}S$ was recorded at room temperature in the range of 200-800 nm (Fig. 5.3d). The absorbance peak observed at 374 nm and the optical band gap was calculated using the Tauc plot (inset of Fig. 5.3d) and was found to be 2.32 eV. [33]

The surface area measurements of the $Ni_{0.5}Co_{0.5}S$ sample using Brunauer-Emmett-Teller (BET) are displayed in Fig. 5.3e. The isotherms for adsorption and desorption have type IV isotherm characteristics corresponding to a complex blend of micro- and mesoporous structures for the $Ni_{0.5}Co_{0.5}S$ sample. The calculated BET-specific surface area and the average diameters of pores were found to be 13.45 m^2/g and 14.27 nm, respectively. The mesopores with a high surface area of the $Ni_{0.5}Co_{0.5}S$ sample will offer better contact with the electrolyte and contribute to better kinetics in electrochemical reactions due to an increase in the concentration of charge carriers at

the surface of the material. The calculated mesopores diameter of the $Ni_{0.5}Co_{0.5}S$ nano-chains is much bigger than the size of OH^- ions in an aqueous KOH electrolyte. [26, 34]

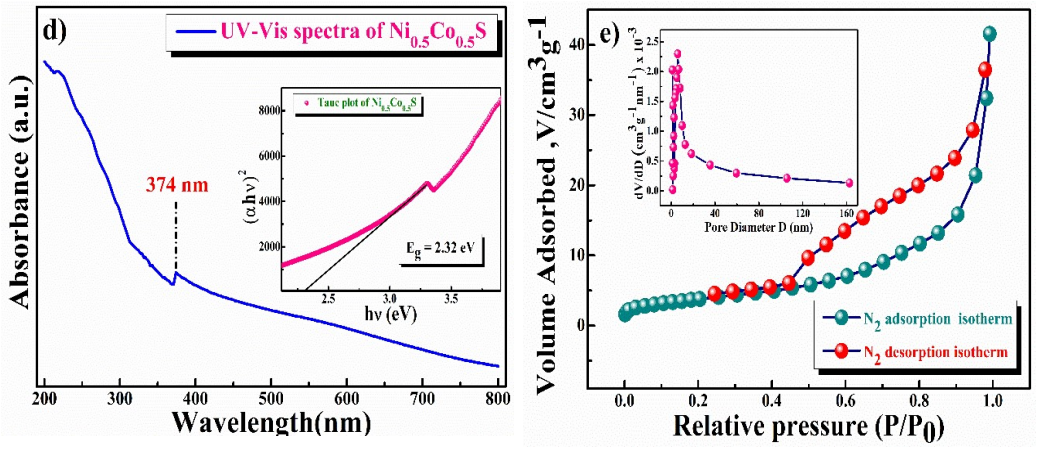

Fig. 5.3 (d) UV-Visible spectra (Tauc plot in the inset) and **(e)** BET nitrogen adsorption/desorption isotherm of $Ni_{0.5}Co_{0.5}S$ nano-chains.

5.3.5 XPS Analysis

The elemental composition and chemical oxidation state of the $Ni_{0.5}Co_{0.5}S$ nano-chains were studied using X-ray photoelectron spectroscopy (XPS). The high-resolution Ni (2*p*) spectrum (Fig. 5.4a) shows $2p_{3/2}$ and $2p_{1/2}$ at 856.74 and 874.34 eV, and the corresponding satellite peaks at 862.46 and 880.23 eV are assigned to Ni^{2+} oxidation state. Likewise, the high-resolution Co (2*p*) spectrum (Fig. 5.4b) shows $2p_{3/2}$ and $2p_{1/2}$ at 782.05 and 797.96 eV, and the corresponding satellite peaks at 786.47 and 802.89 eV are assigned to Co^{2+} oxidation state. The peak observed at 168.98 eV corresponds to S ($2p_{3/2}$) associated with the sulfur-metal bonding and the peak that appeared at 170.12 eV corresponds to S ($2p_{1/2}$) and is attributed to the surface bonding of low-coordination divalent sulfur (S^{2-}). Further, the satellite peak observed at about 162.52 eV corresponds to the binding energies of metal-sulfur bonding (Ni-S and Co-S bonding). Thus, the XPS study confirms the formation of Co^{2+}, $Ni^{2+,}$ and S^{2-}oxidation states in the $Ni_{0.5}Co_{0.5}S$ sample. [16, 19]

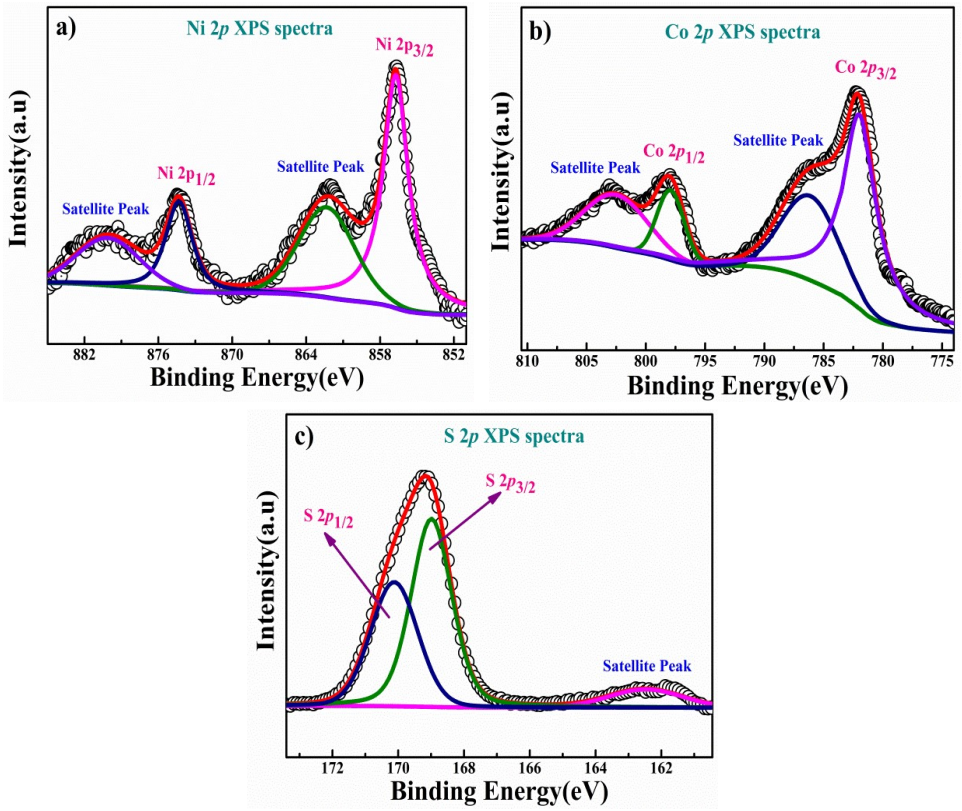

Fig. 5.4 XPS plot of $Ni_{0.5}Co_{0.5}S$ nano-chains, **(a)** Ni (2*p*) spectra, **(b)** Co (2*p*) spectra, and **(c)** S (2*p*) spectra.

5.3.6 FE-SEM and HR-TEM Analysis

Fig. 5.5a shows the SEM image which displays the particle distribution and agglomerated arrangements of the $Ni_{0.5}Co_{0.5}S$ sample containing interconnecting spheres of sub-micron sizes. EDX (energy dispersive X-ray) image shown in Fig. 5.5b, confirms the composition of the material. HR-TEM image shown in Fig. 5.5 (c & d) confirms the formation of the nano-chains arrangement of the $Ni_{0.5}Co_{0.5}S$ sample containing the interconnecting nanosphere. The nano-chains average diameter was ~60 nm arrangements as can be seen in the HRTEM images. Nano-chains structure can provide a fast electron transfer within the material required for a fast/high rate electrochemical charge storage/capacitance of the materials.

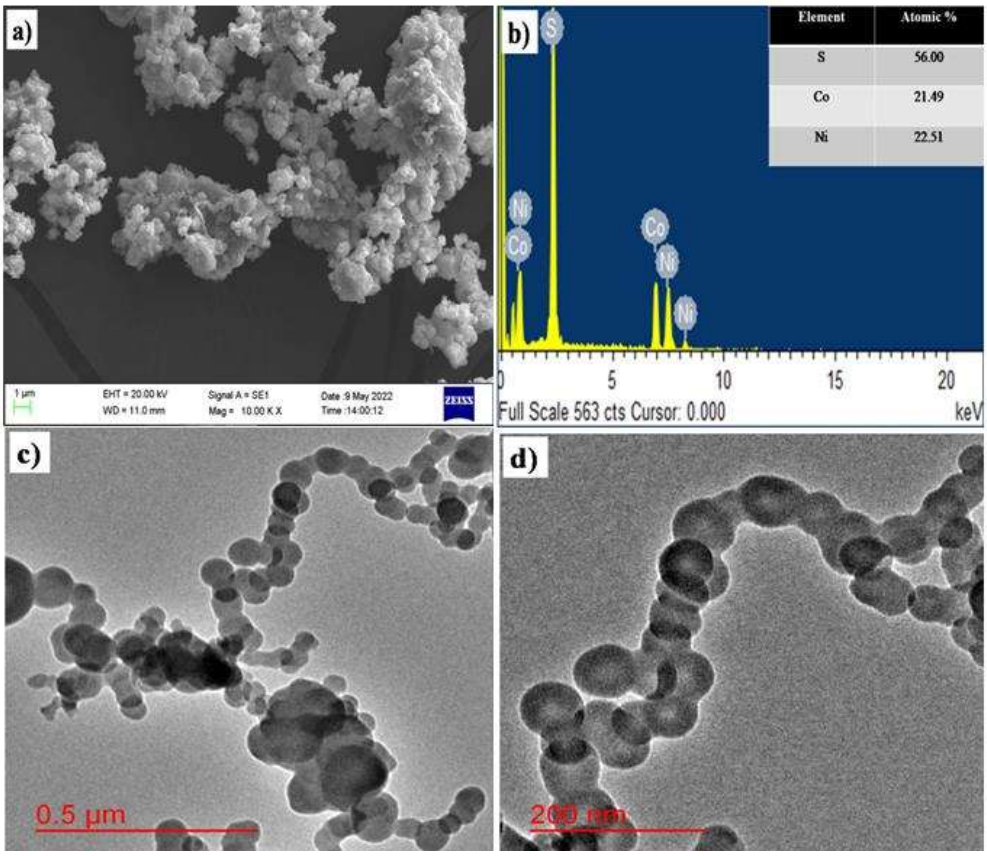

Fig. 5.5 (a) SEM image, **(b)** EDX analysis **(c & d)** HRTEM images of $Ni_{0.5}Co_{0.5}S$ nano-chains.

5.3.7 Electrochemical Studies:

5.3.7.1 Cyclic Voltammetry Analysis

The electrochemical behavior was investigated using galvanostatic charge-discharge and cyclic voltammetry to evaluate the capability and suitability of the material for energy storage as supercapacitors. The charge-storage properties of the $Ni_{0.5}Co_{0.5}S$ electrodes were initially assessed by CV in a three-electrode system where the counter electrode was a platinum electrode, $Ni_{0.5}Co_{0.5}S$ nano-chains coated carbon paper of area $1cm^2$ was used as the working electrode, and saturated Hg/HgO (1 M KOH) as a reference electrode in KOH electrolyte. The CV curves were measured at various KOH concentrations including 0.5, 1, 2, 4 and 6 M. The plot of KOH concentration vs mass-specific capacitance is shown in Fig. 5.6a; the mass-specific capacitances (calculated

using equation 5.4) were found to be 1811, 1863, 2163, 2378 and 2007 F/g at 1 mVs^{-1} in 0.5, 1, 2, 4 and 6 M KOH.

As can be seen in Fig. 5.6a that the specific capacitance initially rises with the increase in OH^- concentration and reaches its maximum capacitance in a 4 M KOH solution and then decreases with a further increase in the OH^- concentration. $Ni_{0.5}Co_{0.5}S$ sample has a higher specific capacitance at 4 M KOH due to the optimum quantity of charged ions trapped/stored on the porous surface. The ionic conductivity of the electrolyte decreases at higher concentrations (> 4 M KOH), which is related to the slow migration of ions caused by the high probability of ion collision and the strong electrostatic interaction between anions and cations leading to the sluggish formation of a double layer or surface absorptions of ions resulting in lower specific capacitance of the material in 6 M KOH electrolyte. [35-38]

$$\boldsymbol{C} = \frac{\int_{E_1}^{E_2} \boldsymbol{i}\,(\boldsymbol{E})\boldsymbol{dE}}{\boldsymbol{2\,m\,v\,(E_2 - E_1)}} \qquad (5.4)$$

In this equation, C is the capacitance in F/g, the integral $\int_{E_1}^{E_2} i\,(E)dE$ is the total voltammetric charge acquired by integrating both positive and negative sweeps in CV, ($E_2 - E_1$) is the width of the potential window (V), m is the mass (g) of active material, and v is the scan rate (V s^{-1}). Although the capacitance values in the forward and backward directions do not precisely match, we have used the average value; as a result, the factor 1/2 is employed to create the holistic picture. One pair of clearly distinct redox peaks, located at +0.20/+0.12V, is visible on the CV curve in Fig. 5.6d (4 M KOH). The pseudocapacitive behavior in conjunction with surface redox (electrosorption) is explained by the curve nature of the CV. [39] Thus non-rectangular and quasi-reversible curves were obtained in the potential range of -0.05 to +0.45 V demonstrating that surface redox intercalation followed pseudocapacitive storage.

Redox peaks are the result of the electrochemical charge transfer reaction resulting interconversion of Co^{2+} to Co^{3+} and Ni^{2+} to Ni^{3+} reversibly through electrosorption (redox) of OH^- ions. The following chemical reaction equation is responsible for the redox-mediated charge storage on the electrode. [26]

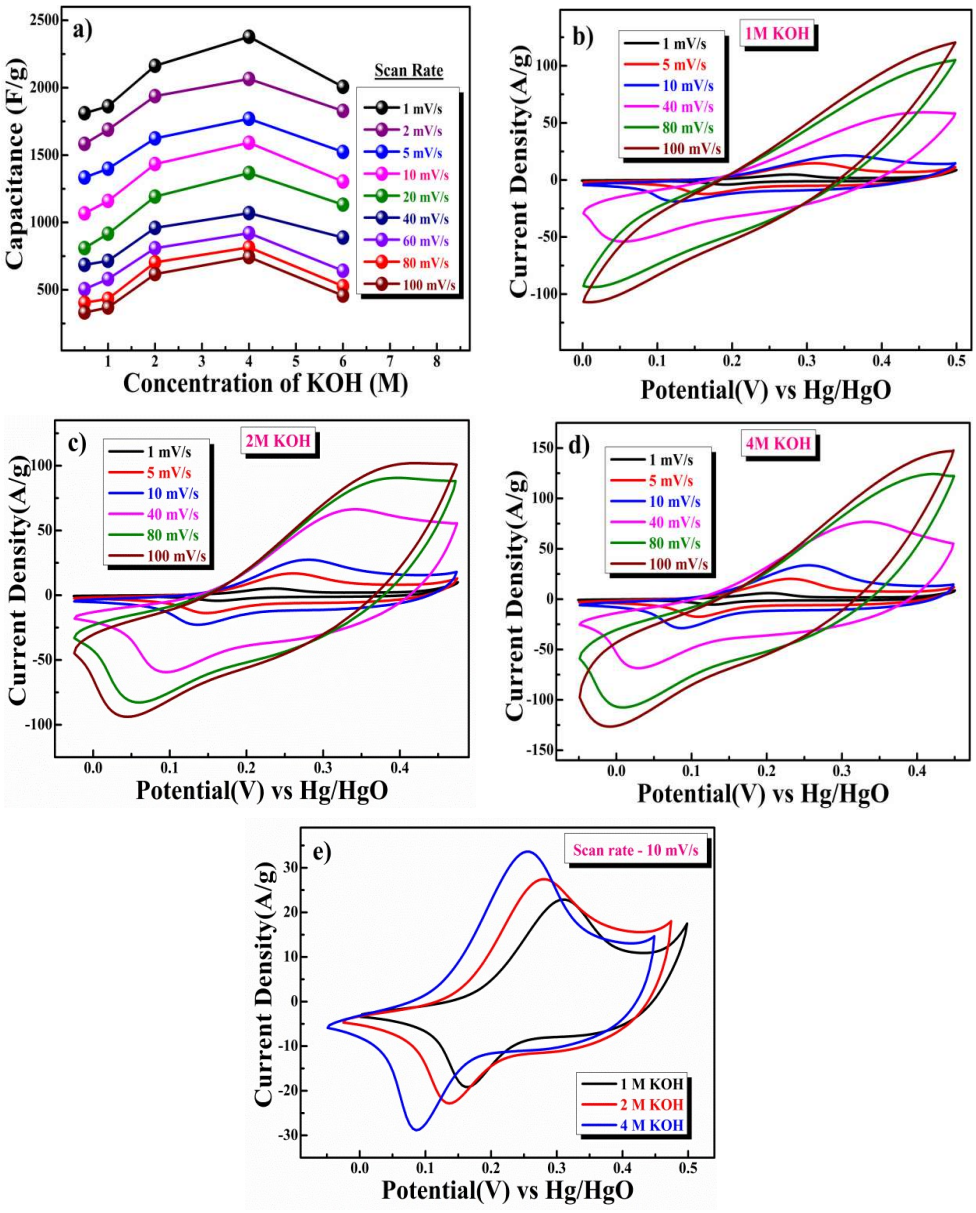

Fig. 5.6 (a) Plot of KOH concentrations vs. specific capacitance at different scan rates. Typical CV curves for $Ni_{0.5}Co_{0.5}S$ electrode in **(b)** 1, **(c)** 2, and **(d)** 4 M KOH solutions at different scan rates of 1-100 mVs^{-1} and **(e)** Comparative CV study in different concentrations of electrolytes at 10 mVs^{-1}.

$$Ni_{0.5}^{2+}\ Co_{0.5}^{2+}\ S\ + OH^{-} = Co_{0.5}^{3+}Ni_{0.5}^{3+}\ S(OH^{-}) + e^{-} \qquad (5.5)$$

Fig. 5.6 (b-d) illustrates typical CV curves for the $Ni_{0.5}Co_{0.5}S$ electrode at various KOH concentrations with scan rates ranging from 1 to 100 mVs^{-1}. Further studies were carried out in 4 M KOH electrolyte only as best activity of the electrode was found in this electrolyte. For 4 M KOH, the capacitance was measured at different scan rates of 1, 5, 10, 20, 40, 80and 100 mVs^{-1} and was found to be 2378, 1770, 1592, 1368, 1069, 815 and 743 F/g.

The specific capacitance decreases as the scan rates increase due to incomplete absorption coupled with surface redox at high scan rates. As the scan rate rises, the cathodic and anodic peaks shifted linearly to a negative and positive potential, respectively. At the same time, the almost unchanged shapes of each curve demonstrated the high reversibility and rapid charge-discharge response of the $Ni_{0.5}Co_{0.5}S$ electrode. Capacitance retention for 4 M KOH drops to 31.2% as the scan rate rises from 1 to 100 mV s^{-1} due to inadequate time for absorption and diffusion of ions into the active surfaces of the electrode at high scan rates. The comparative CV analysis at various electrolyte concentrations, ranging from 1 to 4 M, is shown in Fig. 5.6e. With increasing electrolyte concentration (KOH), redox potential is shifted to a lower value and it is undesirable for high-voltage supercapacitors applications. [26, 35]

5.3.7.2 Determination of Diffusion Coefficient

Fig. 5.6f illustrates a linear relation between cathodic and anodic peak currents concerning the square root of scan rate ($\upsilon^{1/2}$) indicating that the CV curve demonstrates a process regulated by semi-infinite diffusion. The dynamics of electrode diffusion can be better understood by calculating the diffusion coefficient. Using the Randles-Sevick equation (eq. 5.6), the electrode's diffusion coefficient was determined.

$$i_p = 2.686 \times 10^5 \times n^{3/2} A\, D^{1/2}\, C_o\, v^{1/2} \qquad (5.6)$$

In this equation, i_p is peak current (A), n is the number of electrons transferred in the redox reaction (usually ~1), A is the area of the electrode in cm^2, D is diffusion coefficient in cm^2/s, C_o is the concentration of OH^- ion in mol/cm^3, υ is the scan rate in V/s. D was determined to be $3.14 \times 10^{-8} cm^2/s$ for oxidation and $2.50 \times 10^{-8} cm^2/s$ for reduction, respectively.

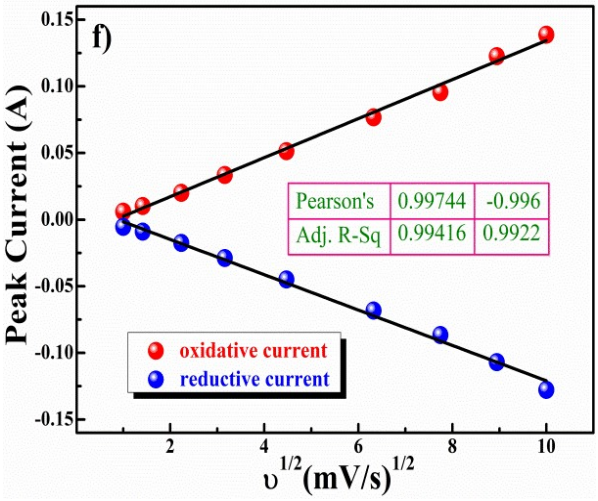

Fig. 5.6 (f) Plot of peak current vs. square root of the scan rate for diffusion kinetics of $Ni_{0.5}Co_{0.5}S$ electrode.

With 1 e^-/OH^- charge transfer associated with reversible intercalation/de-intercalation of OH^- ions, $Ni_{0.5}Co_{0.5}S$ electrode has a theoretical capacity of 1061.86 F/g, in the voltage window of -0.05 to 0.45V. In our investigation, $Ni_{0.5}Co_{0.5}S$ demonstrated a consistent capacitance equal to 2378 F/g at the scan rate of 1 mV/s. Even at the scan rate of 40 mV/S, the $Ni_{0.5}Co_{0.5}S$ electrode demonstrated a capacitance equivalent to 1069 F/g. Thus, the capacitance of $Ni_{0.5}Co_{0.5}S$ can be described as a combination of double-layer formation coupled with diffusion-controlled surface redox reactions. The electrochemical charge storage reaction is depicted in equation 5.7 representing the

contribution of both (1) double-layer formation and (2) diffusion-controlled surface redox processes.

$$Ni_{0.5}^{2+}\ Co_{0.5}^{2+}\ S\ + xOH^{-} + KOH \leftrightarrow K^{+}Ni_{0.5-x}^{2+}\ Ni_{x}^{3+}Co_{0.5-x}^{2+}Co_{x}^{3+}S(OH)_{1+x}^{-} \qquad (5.7)$$

The value of x can vary with the scan rates. The contribution of both (1) double-layer formation and (2) diffusion-controlled surface redox processes are determined in later studies. As we know, the charge storage of the electrode is mainly composed of two parts: the surface-controlled double-layer formation and the diffusion-controlled redox process.

5.3.7.3 Kinetics Studies (Determination of *b* values) and Dunn's Plot Analysis

The charge storage mechanisms/kinetics of the $Ni_{0.5}Co_{0.5}S$ electrode was further evaluated qualitatively using the power law outlined in eq. 5.8. [26, 40]

$$i = av^{b} \qquad (5.8)$$

Where i is the current (A), a & b are adjustable values, and v is the scan rate (V/s). The b value lies between 0.5-1, b = 1 stands for the surface control capacitive reaction or electrosorption while b = 0.5 stands for the semi-infinite diffusion control reaction for battery (intercalative) type material. The slopes of the corresponding log (v) vs. log (i) plot for the oxidative and reductive current's b-values were found to be 0.67 and 0.68, respectively, from Fig. 5.7a, suggesting that current is a linear combination of diffusion-controlled insertion processes and pseudocapacitive processes (diffusion-controlled redox-mediated intercalative processes). The contributions of diffusion-controlled and surface-controlled capacitance processes to the experimental data are assessed using Trasatti's [41] and Dunn's [42] methods. The quantitative voltammetry sweep rate dependency that can determine the capacitive contribution to the current response is

shown in Fig. 5.7b. Diffusion-controlled insertion/intercalation and surface capacitive reactions contribute differently to the current response at a fixed potential. [43]

$$i(\upsilon) = k_1\upsilon + k_2\upsilon^{1/2} \qquad (5.9)$$

For better understanding, eq. 5.9 was modified as

$$\frac{i(\upsilon)}{\upsilon^{1/2}} = \frac{k_1}{\upsilon^{1/2}} + k_2 \qquad (5.10)$$

In eq. 5.10, $k_1\upsilon$ and $k_2\upsilon^{1/2}$ are the current contributions from the surface capacitive and diffusion-controlled intercalation processes, respectively.

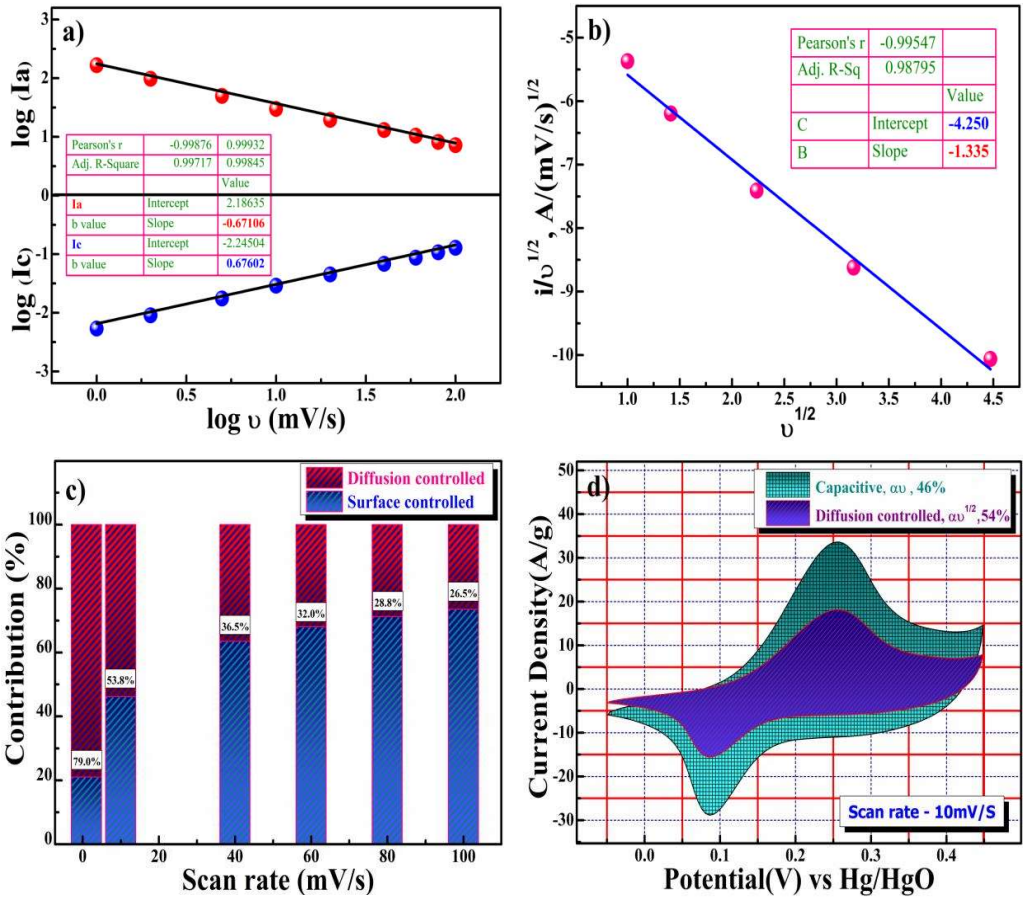

Fig. 5.7 Electrodynamic characteristics of the $Ni_{0.5}Co_{0.5}S$ electrode; **(a)** Plot of the linear relationship between log (peak current) and log (scan rate) at two different scan rate regions, **(b)** Plot of the power law of the charged state at potential and discharged state at a potential, **(c)** Diffusive and capacitive contribution at different scan rates and **(d)** Analysis of kinetic contribution at 10 mVs^{-1}.

Consequently, after calculating k_1 and k_2 from the slope and intercept of the y-axis from linear fit, we can measure their contribution to the current density at the fixed specific potential. [44]

The typical curve $\{(V)/\upsilon^{1/2}$ vs. $\upsilon^{1/2}\}$ in Fig. 5.7c represents the contribution of surface-mediated capacitance and diffusion-controlled intercalative processes at different scan rates. Specific contribution at a 10 mVs^{-1} scan rate is shown in Fig. 5.7d. Surface capacitance or electrosorption was found to contribute 46.0%, whereas diffusion-controlled intercalative contributed around 54.0%.

5.3.7.4 Trassati's Plot Analysis

The amount of charge stored in the outer and inner surfaces was also determined using the Trasatti plot. The total specific capacitance of the electrode, according to Trassati, is influenced by both the inner and outer surface capacitances. This can be expressed as

$$C_{Total} = C_{in} + C_{out}(\text{F/g}) \qquad (5.11)$$

The charge storage method relies on the CV analysis's scan rate. The electrode's total charge storage capacity or capacitance is shown as the y-intercept in Fig. 5.7e, which plots the linear fit of C^{-1} vs. $\upsilon^{1/2}$ at various scan rates. The outer surface capacitance or charge storage of the electrode is represented by the y-intercept in Fig. 5.7f, which illustrates the linear fit of C vs. $\upsilon^{-1/2}$. C_{in} was found to be 1709 F/g (58.6% of the overall capacitance value), C_{out} was found to be 1208 F/g (41.4% of the total capacitance value), and total capacitance value (C_{total}) was found to be 2917 F/g. This confirms that the charge storage or capacitance of the $Ni_{0.5}Co_{0.5}S$ electrodes is a combination of

redox-mediated diffusion-controlled intercalating process and surface absorption processes.

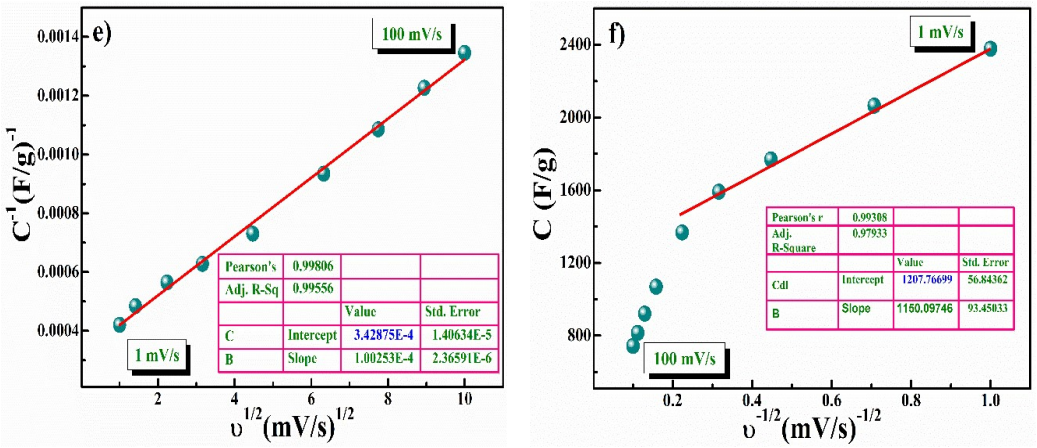

Fig. 5.7 (e, f) Trasatti plot at different scan rates for $Ni_{0.5}Co_{0.5}S$ electrode.

5.3.7.5 Chronoamperometry Charge/Discharge Analysis

To better understand the electrochemical characteristics of charge storage of the $Ni_{0.5}Co_{0.5}S$ electrode, galvanostatic charge-discharge (GCD) studies in 4 M KOH aqueous electrolytes were performed. Using equation 5.12, the specific capacitance of the electrode can be calculated from the charge-discharge curve. [23, 44]

$$Csp = \frac{I\Delta t}{m\Delta V} \qquad (5.12)$$

Where I is the discharge current (A), Δt is the discharge time (s), m is the loading mass of the active material in the electrode (g), and ΔV is the potential window in the charge-discharge measurement (V).

The specific capacitances at current densities of 1, 2, 3, 5, and 10 A/g are shown in Fig. 5.8a as 2190, 1964, 1734, 1310 and 830 F/g, respectively. The GCD, as mentioned above, showed that as current density increases, specific capacitance gradually decreases. The stability of the electrode is seen in Fig. 5.8b (capacitance value vs. cycle number at different current densities). Long-term cyclic stability at 10 A/g for 10,000

cycles is shown in Fig. 5.8c resulting in 84.0% capacity retention. The specific capacitance did not vary significantly from its initial capacitance after 10,000 cycles. After 10000 cycles of continuous charge/discharge, the electrode's coulombic efficiency $\left(\eta = {}^{t_d}/_{t_c}\right)$ was found to be 92.2%, demonstrating the excellent reversibility of the $Ni_{0.5}Co_{0.5}S$ electrode. The comparison of GCD at 1, 2 and 4 M KOH concentrations is shown in Fig. 5.8d. It is evident from the discharge time that, at a current rate of 1 A/g, the electrode delivers a longer discharge time in 4 M KOH electrolytes than it does in 1 and 2 M KOH electrolytes.

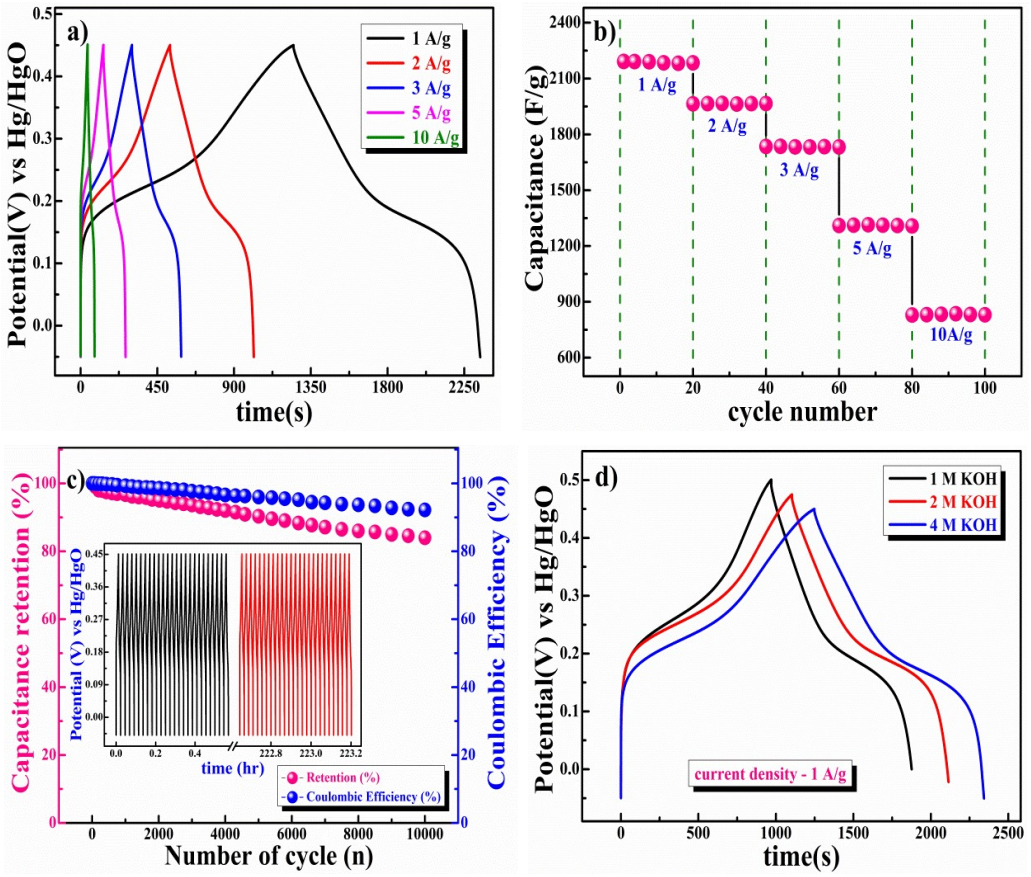

Fig. 5.8 (a) Charge/discharge curve of $Ni_{0.5}Co_{0.5}S$ electrode, **(b)** Capacitance performance of $Ni_{0.5}Co_{0.5}S$ electrode at different constant current density, **(c)** Capacitance retention and coulombic efficiency $Ni_{0.5}Co_{0.5}S$ electrode and **(d)** Comparative study of GCD at 1, 2, and 4 M KOH concentration.

The charge-discharge plot was used to measure the specific capacitance of the electrode, which is 1812, 2020 and 2190 F/g for concentrations of 1, 2 and 4 M KOH electrolyte, respectively. Through comparative GCD observations, an increase in specific capacitance value from 1 to 4 M KOH concentration is confirmed, which is similar to the findings of the CV results.

5.3.7.6 Analysis of Electrochemical Impedance Spectroscopy (EIS)

The electrochemical impendence spectra (EIS) were studied (before and after 10000 repeated charge-discharge cycles) to evaluate the electrode kinetics and interface resistance at an open circuit potential in the frequency range of 100 kHz to 0.1 Hz. The Nyquist plot (Fig. 5.8e**)** shows the impedance characteristic as a function of frequency, which may be divided into two parts: a depressed arc corresponding to faradaic responses in the high-frequency region followed by a straight line in the low-frequency region, indicating a fast OH^- ion diffusion-controlled process. Further, the impedance contribution was attributed to the impedance distributions over internal series resistance (R_s), charge transfer resistance (R_{ct}), and Warburg impedance (R_w). The internal series resistance (R_s) is represented by the point at which the curve intersects the real axis in the high-frequency region, which includes the resistance of active material, electrolyte, and connected wires at the electrode-electrolyte interface. The R_s and R_{ct} values for the $Ni_{0.5}Co_{0.5}S$ electrode were 1.01 Ω and 0.72 Ω, respectively. Lower-frequency data show the warburg diffusion resistance for the $Ni_{0.5}Co_{0.5}S$ electrode. [45] Based on the EIS spectra, the $Ni_{0.5}Co_{0.5}S$ electrode shows good electrochemical stability after 10,000 consecutive charge-discharge cycles compared to the initial. The Bode plot in Fig. 5.8f depicts the electrode's phase angle concerning the electrode's applied frequency. The $Ni_{0.5}Co_{0.5}S$ electrode's phase angles were 52.2° at the beginning and 45.48° at the end of 10,000 cycles, respectively. The pseudocapacitive charge storage capacity of the

$Ni_{0.5}Co_{0.5}S$ electrode is confirmed by the lower phase angle (about 50°), which is in good accord with the Nyquist plot. [29, 45]

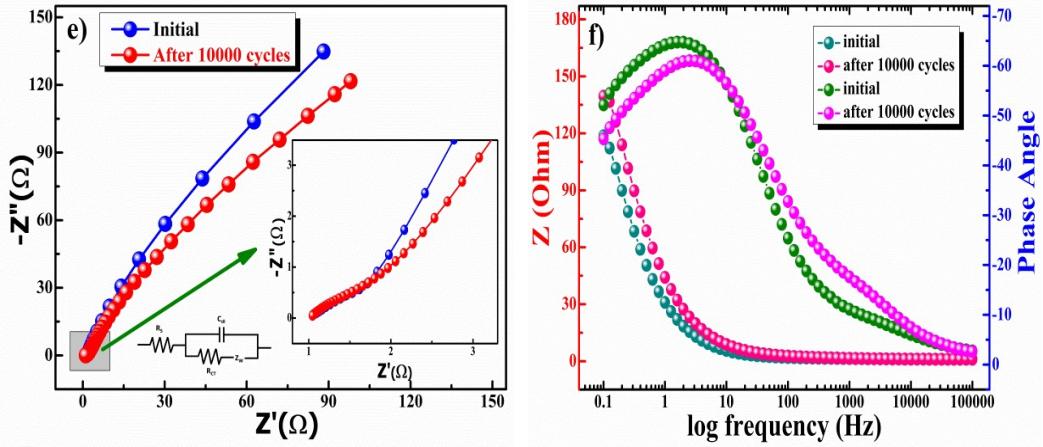

Fig. 5.8 (e) Nyquist and **(f)** Bode plot of $Ni_{0.5}Co_{0.5}S$ electrode at 10 mV between 0.1 Hz and 100 kHz (inset displays enlarged view of Nyquist plot at high-frequency region).

5.3.7.7 Electrochemical Charge Storage Behaviour in Neutral Na_2SO_4 Electrolyte

The charge storage behavior of $Ni_{0.5}Co_{0.5}S$ electrodes in a neutral 0.5 M Na_2SO_4 electrolyte has also been studied. In Fig. 5.9a, the CV curve at different scan rates shows well-separated redox peaks (+0.64/+0.52 V at $1mVs^{-1}$ scan rate). The calculated specific capacitance (which is the function of scan rate) for the $Ni_{0.5}Co_{0.5}S$ electrode in 0.5 M Na_2SO_4 electrolyte is 489, 343, 245, 165, 113 and 98 F/g at 1, 5, 10, 40, 80 and 100 mVs^{-1}scan rates, respectively. Fig. 5.9b shows the results of the quantitative galvanostatic charge/discharge measurements, and the results were found to be 434, 368, 270, 175 and 110 F/g at 1, 2, 3, 5 and 10 A/g, respectively. A comparison study investigated the anion's effects on the electrolyte.

The $Ni_{0.5}Co_{0.5}S$ electrode's comparative CV curve in 0.5 M Na_2SO_4 and 4 M KOH electrolytes is shown in Fig. 5.9c. From KOH to Na_2SO_4 electrolyte, there were changes in the redox peaks positions. Additionally, it was found that the redox peaks in 4 M

KOH were more dominant than those in 0.5 M Na_2SO_4; this could be due to the size difference between the hydration radii of sulfate ions (3.79 Å) and hydroxyl ions (3 Å).

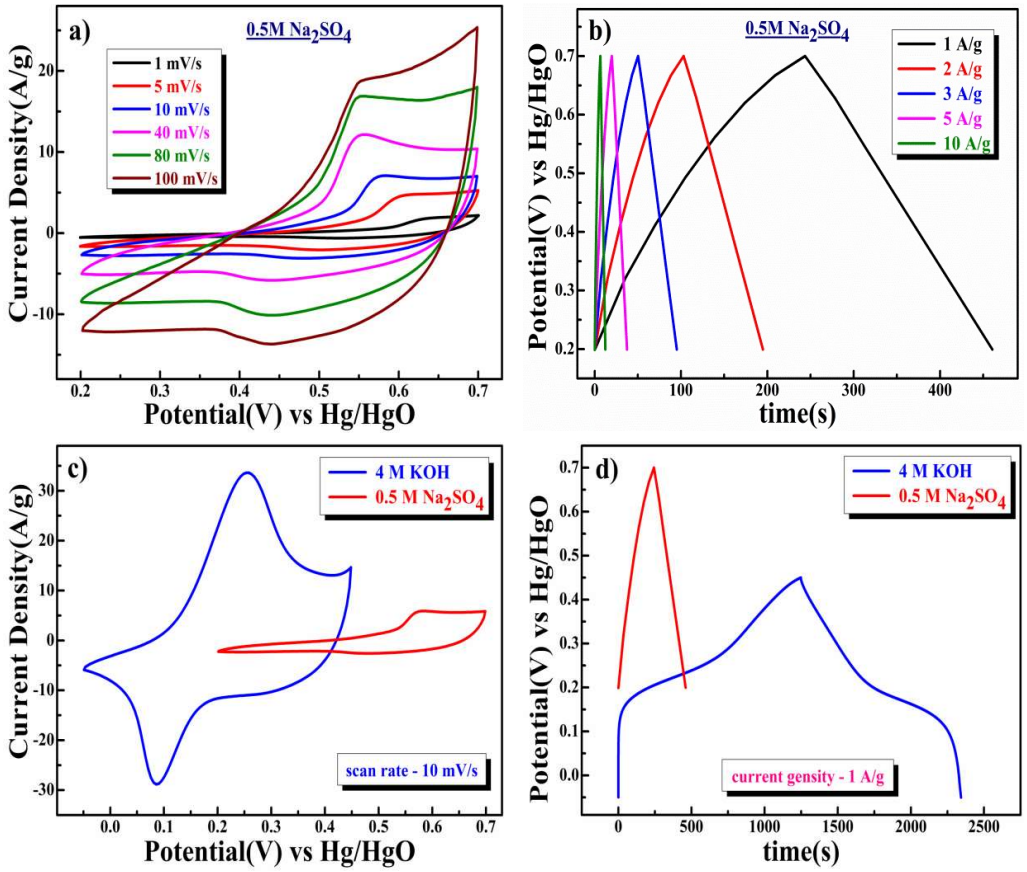

Fig. 5.9 (a) CV and **(b)** GCD plot of $Ni_{0.5}Co_{0.5}S$ electrode in 0.5 M Na_2SO_4 electrolyte, **(c)** Comparative CV diagram of $Ni_{0.5}Co_{0.5}S$ electrode in 4 M KOH and 0.5 M Na_2SO_4 electrolyte at 10 mVs^{-1}, and **(d)** Comparative charge/discharge curve of $Ni_{0.5}Co_{0.5}S$ electrode in KOH and Na_2SO_4 medium at 1 A/g.

The larger size of SO_4^{2-} results in slow kinetic in diffusion-controlled processes resulting in lower charge storage in neutral Na_2SO_4 electrolyte. Moreover, the CV curve's current response is also in accordance due to the higher OH^- ion molar conductance (198 $cm^2\Omega\ mol^{-1}$) in the KOH electrolyte compared to SO_4^{2-} ion conductivity (79.8 $cm^2\Omega\ mol^{-1}$) in Na_2SO_4. [34, 37] The quantitative capacitance of the electrode was measured using GCD experiments in 0.5 M Na_2SO_4 and 4 M KOH electrolytes. The electrode delivers a longer discharge time in 4 M KOH than in 0.5 M

Na_2SO_4 electrolyte at a current rate of 1 A/g, as shown in Fig. 5.9d (see the discharge time). These investigations confirm the excellent electrode performance of the electrode in aqueous KOH electrolyte.

5.3.7.8 Asymmetric Full Cell Test of $Ni_{0.5}Co_{0.5}S$//AC (CV, GCD and Cyclic Stability)

To explore the real applicability of the $Ni_{0.5}Co_{0.5}S$ electrode, the two-electrode full cell was fabricated in ASC mode in a 4 M KOH electrolyte where AC was employed as a counter electrode. To determine the maximum specific capacitance during the full-cell test, the storage capacities of the positive and negative electrodes must be balanced using eq. 5.13.

$$\frac{1}{C_{total}} = \frac{1}{C_{positive}} + \frac{1}{C_{negative}} \qquad (5.13)$$

Equation 5.14 determines the mass ratio (m+/m-) of the positive and negative electrode materials to balance the cell's capacity to store charges.

$$\frac{m^+}{m^-} = \frac{C_- \times \Delta E_-}{C_+ \times \Delta E_+} \qquad (5.14)$$

m^+,m^-, C_+, C_-, ΔE_+, ΔE_- are mass loading on the electrode, specific capacitance, and potential window of positive and negative electrodes estimated by single electrode measurements. [34, 46]

With a fixed scan rate (10 mV/s), separate CV curves for the $Ni_{0.5}Co_{0.5}S$ (positive electrode) and AC (negative electrode) are shown in Fig. 5.10a with a single operating potential window range. The contribution in capacitance due to the AC electrode is extracted when calculating the electrochemical charge storage capacity of the $Ni_{0.5}Co_{0.5}S$ electrode because AC is used to increase the conductivity of the active electrode. Thus the obtained data shows only the capacitive value of the $Ni_{0.5}Co_{0.5}S$ electrode. For the asymmetric cell, the calculated mass ratio (m^+/m^-) was 1.0:3.6, and

the active material's weight was found to be ~4.0 mg (excluding the weight of activated carbon and PVDF).

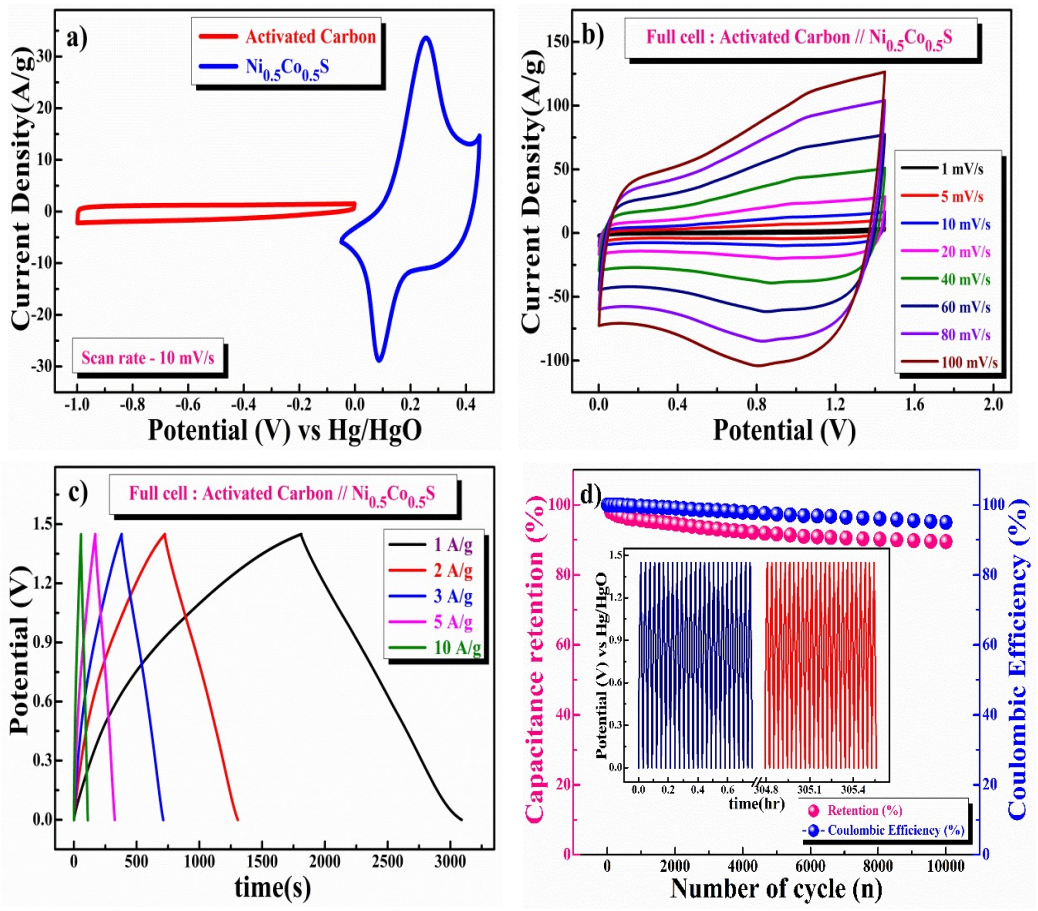

Fig. 5.10 (a) Separate CV plots for activated carbon and $Ni_{0.5}Co_{0.5}S$ electrode in 4 M KOH Electrolyte 10 mV/s, **(b)** CV at different scan rates, **(c)** Charge-discharge at different current rates, and **(d)** Capacitance retention and coulombic efficiency.

Fig. 5.10b shows the CV plot of two-electrode asymmetric supercapacitor cell (ASCs) $Ni_{0.5}Co_{0.5}S$//AC, at scan rates ranging from 1 to 100 mVs^{-1} in the potential window 0 to 1.5 V. Fig. 5.10c depicts the full cell's galvanostatic charge/discharge profile at different current densities. The specific capacitances of ASCs calculated from GCD curves were found to be 881, 801, 685, 534.5 and 369 F/g at constant current densities of 1, 2, 3, 5 and 10 A/g, respectively. The $Ni_{0.5}Co_{0.5}S$ electrode//AC full cell, as shown in Fig. 5.10d, has exceptional long-term cycling stability, with 89.5% capacity retention after

10000 cycles. Further, after 10000 cycles, the $Ni_{0.5}Co_{0.5}S$ electrode//AC full cell's coulombic efficiency has lost merely 5% of its initial value.

5.3.7.9 Electrochemical Impedance Spectroscopy (EIS) of $Ni_{0.5}Co_{0.5}S$//AC Full Cell

Fig. 5.10e and 5.10f show the EIS (Nyquist and Bode) plots at an open circuit potential in the frequency range of 100 kHz to 0.1 Hz, confirming the superior charge transfer, higher specific capacitance and excellent retention of the electronic structure of the $Ni_{0.5}Co_{0.5}S$ electrode//AC full cell in ASC mode. However, a slight reduction in capacity is due to the partially irreversible nature of the electrode, which was shown during the cycling test. The EIS result corroborates the evidence for cycling stability by demonstrating a slight difference in the cell's internal and charge transfer resistances before and after the cycling test.

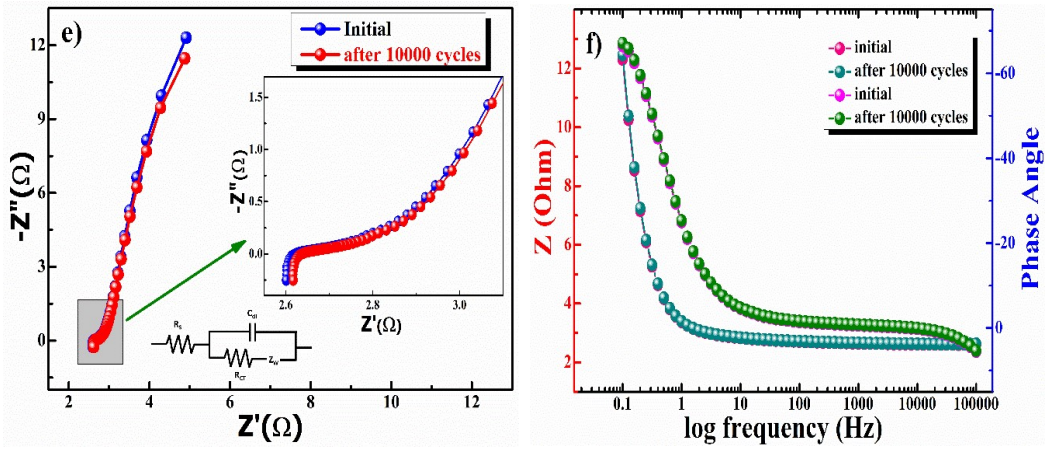

Fig. 5.10 (e) Nyquist and **(f)** Bode plot at 10 mV at initial cycle and after 10000 cycles of full cell formation.

5.3.7.10 Study of Energy Density vs Power Density of $Ni_{0.5}Co_{0.5}S$//AC Full Cell

Equations 5.15 and 5.16 were utilized to calculate the power and energy density of the ASC.

$$P(W/kg) = \frac{E \text{ X } 3600}{t_{dis}} \qquad (5.15)$$

$$E(Wh/kg) = \frac{1}{2}\frac{C_{ASC}}{3.6}\Delta V^2 \qquad (5.16)$$

Where C_{sp} is specific capacitance, ΔV is the operating voltage window, and $t_{dis}$is discharge time. Fig. 5.10g displays the Ragone plot (energy density vs. power density) of the $Ni_{0.5}Co_{0.5}S$ electrode//AC full-cell compared to earlier reported nickel, cobalt and sulfide-based supercapacitors.

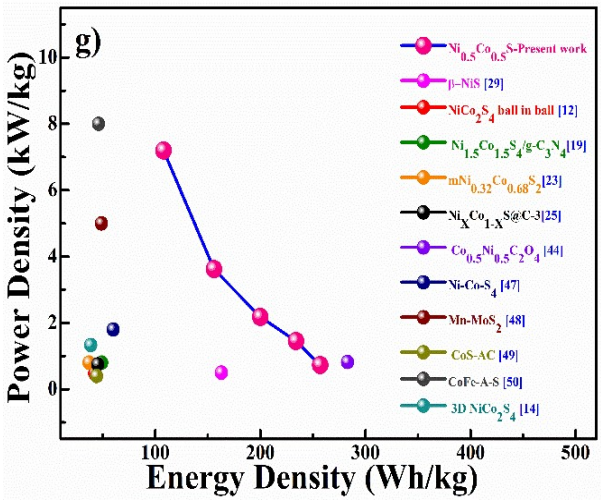

Fig. 5.10 (g) Ragone plot of the $Ni_{0.5}Co_{0.5}S$//AC full cell in ASC mode in comparison with reported supercapacitor devices.

The ASC resultant values confirm the highest energy density equivalent of 257 Wh/kg and power density equivalent of 0.73 kW/kg at 1 A/g current density. When the current density was raised to 10 A/g, the maximum power density of 7.20 kW/kg was obtained and the energy density was reduced to 108 Wh/kg. A literature review of several nanostructured sulfide-based electrodes for supercapacitor applications, such as specific capacitance, capacity retention, energy and power density is shown in **Table 5.1**.

Table 5.1. Displays the Ragone plot of the $Ni_{0.5}Co_{0.5}S$ electrode//AC (ASC) full cell compared with reported supercapacitor devices.

Material	Energy density (Wh/kg)	Power density (kW/kg)	Cycling stability (%) after "n" cycles	Capacitance (three-electrode system)	Ref.
β -NiS	163	0.5	90.0%, 2500	780 F/g at 1 A/g	[29]
$NiCo_2S_4$ spheres	42.3	0.48	78.6%, 10000	119 F/g at 5 mV/s	[12]
$Ni_{1.5}Co_{1.5}S_4$/g-C_3N_4	49.0	0.8	95.5%, 8000	138 at 1 A/g	[19]
$mNi_{0.32}Co_{0.68}S_2$	37	0.8	66.0%, 1000	91 at 2 A/g	[23]
$Ni_XCo_{1-X}S$@C-3	45.31	0.75	91.0%, 8000	145 F/g at 1 A/g	[25]
$Co_{0.5}Ni_{0.5}C_2O_4$	283	0.82	90.7%, 2500	796 F/g at 1 A/g	[44]
Ni-Co-S_4	60	1.8	90.1%, 10000	133 F/g at 2 A/g	[47]
Mn-MoS_2	48.8	5.0	77.0%, 5000	88 F/g at 1 A/g	[48]
CoS-AC//AC	44.2	0.4	77.5%, 2000	118 F/g at 1 A/g	[49]
FeCo-A-S	46.1	8.0	79.3%, 10000	200 F/g at 1 A/g	[50]
3D $NiCo_2S_4$	38.64	1.33	72.7%, 10000	112 F/g at 1.6 A/g	[14]
$Ni_{0.5}Co_{0.5}S$ nano-chains	**257**	**0.73**	**89.5%, 10000**	**881 F/g at 1 A/g**	**Present work**

5.4 Conclusions

In summary, the single-phase hexagonal $Ni_{0.5}Co_{0.5}S$ nano-chains consisting of interconnected nano-spheres were synthesized using a simple H_2S-mediated two-phase (gas diffusion in liquid) precipitation route in an aqueous medium. $Ni_{0.5}Co_{0.5}S$ nano-chains formed in a single phase due to the result of gradual diffusion of H_2S gas into the liquid phase resulting in controlled precipitation of the solid phase. The XRD pattern confirms the formation of single-phase hexagonal $Ni_{0.5}Co_{0.5}S$ nano-crystalline material, and the average crystallite size estimated using the Debye Scherrer equation was approximately 21 nm. Nano-chains structure can provide a fast electron transfer within the material required for a fast/high rate electrochemical charge

storage/capacitance of the materials. With a specific capacitance of 2378 F/g at 1 mVs^{-1} in CV and 2190 F/g at a current density of 1 A/g in the GCD test, in the potential window of -0.05 to 0.45 V, the $Ni_{0.5}Co_{0.5}S$ electrode demonstrated excellent pseudocapacitive charge storage performance. Furthermore, a predominant redox-mediated diffusion-controlled pseudocapacitive mechanism blend with surface capacitance (electrosorption) seems to be the reason behind the high charge storage capacity of the materials, as the intercalative (inner) and surface (outer) charges stored by the $Ni_{0.5}Co_{0.5}S$ electrodes were found to be 54.0%, and 46.0%, respectively. The $Ni_{0.5}Co_{0.5}S$ //AC full cell achieved a maximum energy density of 257 Wh/kg and a power density of 0.73 kW/kg in the 1.5 V voltage window in 4 M KOH electrolyte at 1 A/g current density. Results demonstrate that charge storage behavior and the capacitance value are comparable to or superior to most of the reported transition-metal nanostructured pseudocapacitors/supercapacitors. These findings demonstrate the potential of the $Ni_{0.5}Co_{0.5}S$ nano-chains to be a pseudocapacitive electrode for large-scale energy storage applications.

5.5 References

1. Lee, Y.J., et al., *Synthesis and electrochemical properties of nickel sulfide/carbon composite as anode material for lithium-ion and sodium-ion batteries.* International Journal of Energy Research, 2022. **46**(12): p. 16883-16895.
2. Feng, N., et al., *Growth of nanostructured nickel sulfide films on Ni foam as high-performance cathodes for lithium ion batteries.* Physical Chemistry Chemical Physics, 2013. **15**(24): p. 9924-9930.
3. Zhang, X., et al., *Cobalt sulfide embedded carbon nanofibers as a self-supporting template to improve lithium ion battery performances.* Electrochimica Acta, 2021. **366**: p. 137351.
4. Wang, B., et al., *Boosting transport kinetics of cobalt sulfides yolk–shell spheres by anion doping for advanced lithium and sodium storage.* ChemSusChem, 2020. **13**(16): p. 4078-4085.
5. Liu, Y., S. Niu, and R. Hu, *Preparation and supercapacitive performance of manganese-cobalt sulfide/silver nanowires/graphene ternary nanocomposites.* Journal of Materials Science: Materials in Electronics, 2021. **32**(11): p. 14337-14346.
6. Javed, M.S., et al., *Construction of highly dispersed mesoporous bimetallic-sulfide nanoparticles locked in N-doped graphitic carbon nanosheets for high energy density hybrid flexible pseudocapacitors.* Journal of Materials Chemistry A, 2019. **7**(29): p. 17435-17445.
7. Pallavolu, M.R., et al., *Self-Assembled Hierarchical Silkworm-Type Bimetallic Sulfide (NiMo3S4) Nanostructures Developed on Sg-C3N4 Sheets: Promising*

Electrode Material for Supercapacitors. ACS Applied Energy Materials, 2023. **6**(2): p. 812-821.

8. Shao, Q., et al., *Vulcanization Conditions of Bimetallic Sulfides Under Different Sulfur Sources for Supercapacitors: A Review.* Journal of Electronic Materials, 2023. **52**(3): p. 1769-1784.
9. Fang, G., et al., *Observation of pseudocapacitive effect and fast ion diffusion in bimetallic sulfides as an advanced sodium-ion battery anode.* Advanced Energy Materials, 2018. **8**(19): p. 1703155.
10. Chen, X., et al., *Nickel and cobalt sulfide-based nanostructured materials for electrochemical energy storage devices.* Chemical Engineering Journal, 2021. **409**: p. 127237.
11. Li, D., Y. Gong, and C. Pan, *Facile synthesis of hybrid CNTs/NiCo2S4 composite for high performance supercapacitors.* Scientific reports, 2016. **6**(1): p. 29788.
12. Shen, L., et al., *Formation of nickel cobalt sulfide ball-in-ball hollow spheres with enhanced electrochemical pseudocapacitive properties.* Nature communications, 2015. **6**(1): p. 6694.
13. Wu, P., et al., *A low-cost, self-standing NiCo2O4@ CNT/CNT multilayer electrode for flexible asymmetric solid-state supercapacitors.* Advanced Functional Materials, 2017. **27**(34): p. 1702160.
14. Lu, F., et al., *Engineering sulfur vacancies and impurities in NiCo2S4 nanostructures toward optimal supercapacitive performance.* Nano Energy, 2016. **26**: p. 313-323.

15. Han, Y., et al., *Multidimensional structure of CoNi 2 S 4 materials: structural regulation promoted electrochemical performance in a supercapacitor.* RSC advances, 2020. **10**(13): p. 7541-7550.

16. Hu, W., et al., *CoNi2S4 nanosheet arrays supported on nickel foams with ultrahigh capacitance for aqueous asymmetric supercapacitor applications.* ACS applied materials & interfaces, 2014. **6**(21): p. 19318-19326.

17. Chen, L., et al., *Construction of CoNi2S4 hollow cube structures for excellent performance asymmetric supercapacitors.* Applied Surface Science, 2021. **570**: p. 151174.

18. Zheng, X., et al., *High-Performance Asymmetric Supercapacitors Based on the Ni 1. 5 Co 1. 5 S4@ CNTs Nanocomposites.* Nano, 2020. **15**(10): p. 2050136.

19. Jin, F., et al., *Synthesis of hierarchical porous Ni1. 5Co1. 5S4/g-C3N4 composite for supercapacitor with excellent cycle stability.* Nanomaterials, 2020. **10**(9): p. 1631.

20. Yu, L., et al., *Formation of NixCo3− xS4 hollow nanoprisms with enhanced pseudocapacitive properties.* Angewandte Chemie, 2014. **126**(14): p. 3785-3788.

21. Yang, F., et al., *NixCo3− xS4@ NiCo2O4 hybrid composites as supercapacitors electrode material.* Materials Letters, 2017. **191**: p. 101-104.

22. Cao, D., et al., *In situ N-doped carbon modified (Co 0.5 Ni 0.5) 9 S 8 solid-solution hollow spheres as high-capacity anodes for sodium-ion batteries.* Journal of Materials Chemistry A, 2019. **7**(14): p. 8268-8276.

23. Jin, L., et al., *Synthesis of Mesoporous CoS2 and Ni x Co1–x S2 with Superior Supercapacitive Performance Using a Facile Solid-Phase Sulfurization.* ACS applied materials & interfaces, 2017. **9**(42): p. 36837-36848.

24. Li, G. and C. Xu, *Hydrothermal synthesis of 3D NixCo1− xS2 particles/graphene composite hydrogels for high performance supercapacitors.* Carbon, 2015. **90**: p. 44-52.

25. Huang, C., et al., *Metal organic frameworks derived Ni-doped hierarchical NiXCo1-XS@ C bundled-like nanostructures for enhanced supercapacitors.* Electrochimica Acta, 2022. **406**: p. 139872.

26. Jian, C., et al., *Ni Doped CoS2 as Cathode Catalysts with Enhanced Performances for Lithium− Oxygen Batteries.* Int. J. Electrochem. Sci, 2022. **17**(220744): p. 2.

27. Yang, J., et al., *Hybrid NiCo 2 S 4@ MnO 2 heterostructures for high-performance supercapacitor electrodes.* Journal of Materials Chemistry A, 2015. **3**(3): p. 1258-1264.

28. Wang, D., et al., *Well-dispersed NiCoS2 nanoparticles/rGO composite with a large specific surface area as an oxygen evolution reaction electrocatalyst.* Rare Metals, 2021. **40**(11): p. 3156-3165.

29. Kushwaha, V., et al., *Nanocrystalline β-NiS: a redox-mediated electrode in aqueous electrolyte for pseudocapacitor/supercapacitor applications.* Physical Chemistry Chemical Physics, 2023. **25**(1): p. 555-569.

30. Zhu, T., et al., *Synthesis of NiCo 2 S 4-based nanostructured electrodes supported on nickel foams with superior electrochemical performance.* Journal of materials science, 2016. **51**: p. 1903-1913.

31. Dong, M., et al., *One-step potentiostatic electrodeposition of cross-linked bimetallic sulfide nanosheet thin film for supercapacitors.* Ionics, 2020. **26**: p. 4095-4102.

32. Jabeen, N., et al., *Unique core–shell nanorod arrays with polyaniline deposited into mesoporous NiCo2O4 support for high-performance supercapacitor electrodes.* ACS applied materials & interfaces, 2016. **8**(9): p. 6093-6100.

33. Ahmed, S., et al., *Solvent-free synthesis of NiCo2S4 having the metallic nature.* Frontiers in Chemistry, 2022. **10**: p. 1027024.

34. Mishra, N.K., et al., *NiC2O4· 2H2O Nanoflakes: A Novel Redox-mediated Intercalative Pseudocapacitive Electrode for Supercapacitor Applications in Aqueous KOH and Neutral Na2SO4 electrolytes.* ChemistrySelect, 2022. **7**(21): p. e202201134.

35. Gupta, A., et al., *SrFeO 3− δ: a novel Fe 4+↔ Fe 2+ redox mediated pseudocapacitive electrode in aqueous electrolyte.* Physical Chemistry Chemical Physics, 2022. **24**(18): p. 11066-11078.

36. Pattanayak, B., et al., *Ion accumulation-induced capacitance elevation in a microporous graphene-based supercapacitor.* RSC advances, 2022. **12**(42): p. 27082-27093.

37. Pal, B., et al., *Electrolyte selection for supercapacitive devices: a critical review.* Nanoscale Advances, 2019. **1**(10): p. 3807-3835.

38. Zhang, L., et al., *Magnetic field-induced capacitance change in aqueous carbon-based supercapacitors.* Cell Reports Physical Science, 2021. **2**(6).

39. Evanko, B., et al., *Redox-enhanced electrochemical capacitors: status, opportunity, and best practices for performance evaluation.* ACS Energy Letters, 2017. **2**(11): p. 2581-2590.

40. Fleischmann, S., et al., *Pseudocapacitance: from fundamental understanding to high power energy storage materials.* Chemical Reviews, 2020. **120**(14): p. 6738-6782.

41. Ardizzone, S., G. Fregonara, and S. Trasatti, *"Inner" and "outer" active surface of RuO2 electrodes.* Electrochimica Acta, 1990. **35**(1): p. 263-267.

42. Wang, J., et al., *Pseudocapacitive contributions to electrochemical energy storage in TiO2 (anatase) nanoparticles.* The Journal of Physical Chemistry C, 2007. **111**(40): p. 14925-14931.

43. Kumar, R. and M. Bag, *Quantifying capacitive and diffusion-controlled charge storage from 3D bulk to 2D layered halide perovskite-based porous electrodes for efficient supercapacitor applications.* The Journal of Physical Chemistry C, 2021. **125**(31): p. 16946-16954.

44. Mishra, N.K., et al., *Synthesis, characterizations, and electrochemical performances of highly porous, anhydrous Co0. 5Ni0. 5C2O4 for pseudocapacitive energy storage applications.* ACS omega, 2022. **7**(2): p. 1975-1987.

45. Singh, A.N., et al., *Effect of strontium doping on the electrochemical pseudocapacitance of Y 1− x Sr x MnO 3− δ perovskites.* Physical Chemistry Chemical Physics, 2023. **25**(1): p. 326-340.

46. Subramani, K., et al., *All-solid-state asymmetric supercapacitors based on cobalt hexacyanoferrate-derived CoS and activated carbon.* RSC advances, 2017. **7**(11): p. 6648-6659.

47. Chen, W., C. Xia, and H.N. Alshareef, *One-step electrodeposited nickel cobalt sulfide nanosheet arrays for high-performance asymmetric supercapacitors.* ACS nano, 2014. **8**(9): p. 9531-9541.

48. Singha, S.S., et al., *Mn incorporated MoS2 nanoflowers: A high performance electrode material for symmetric supercapacitor.* Electrochimica Acta, 2020. **338**: p. 135815.

49. Xu, T., et al., *One-pot synthesis of a CoS-AC electrode in a redox electrolyte for high-performance supercapacitors.* Journal of Applied Electrochemistry, 2019. **49**: p. 1069-1077.

50. Yan, S.-x., et al., *Asymmetric, flexible supercapacitor based on Fe–Co Alloy@ sulfide with high energy and power density.* ACS Applied Materials & Interfaces, 2021. **13**(42): p. 49952-49963.